Dynamical Decoupling of Nitrogen-Vacancy Electron Spins in Diamond and Nanodiamond

BACHELORARBEIT

zur Erlangung des akademischen Grades
Bachelor of Science
(B. Sc.)
im Fach Physik

eingereicht an der
Mathematisch-Naturwissenschaftlichen Fakultät I
Institut für Physik
Humboldt-Universität zu Berlin

von
Herr Richard Kullmann
geboren am 17.07.1996 in Berlin-Pankow

Gutachter:

1. *Prof. Dr. Oliver Benson*
2. *Prof. Dr. Kurt Busch*

eingereicht am: *23. Januar 2018*

Contents

1 Introduction

By the end of the 20th century, the possibility of creating and manipulating single quantum systems has given rise to a manifold of new scientific and technological developments. Among these, quantum magnetic field imaging has attracted a lot of attention due to the unprecedented spatial and quantitative resolution that has been achieved through it. This technique is based on the idea to bring a solid state electronic spin close to the magnetic target and optically measure the Zeeman

~~shift of its energy sublevels, thus using it as a magnetic field sensor. However, the successful implementation requires a stable and controllable~~ quantum system which can be read out easily. Recently, it has been shown that the Nitrogen-Vacancy (NV) defect center in diamond satisfies these conditions and is a promising candidate for the realization of this technique. In order to achieve a high stability, meaning long coherence times, it is crucial to decouple the spin from interactions with the environment. This can be accomplished through dynamical decoupling techniques. The goal oft this thesis was the implementation of different decoupling techniques and the performance on single NV spins in a Nanodiamond and a bath of NV spins from a Bulk diamond, respectively.

2 Theory

2.1 Diamond

~~As NVs~~ are embedded in the diamond crystal lattice, it is important to study the properties of diamond. Pure diamond consists only of carbon atoms which are arranged in an fcc structure with a two-atomic basis, the basis being formed by carbon atoms at the positions $(0,0,0)$ and $(^1/_4,^1/_4,^1/_4)$. The equilibrium distance of $R_0 = 3,57\,\text{Å}$ results in a bandgap of $E_g = 5,5\,\text{eV}$[17].

2.1.1 Type classification of diamond

In nature, almost no diamond is absolutely pure. So, the Type classification system is based on the occurrence of the two most common impurities: boron or nitrogen ~~substituting carbon atoms in the lattice.~~ Diamonds are classified into type I and II. Type I diamonds contain enough N atoms to be detected by IR absorption spectroscopy while the concentration of N in type II diamonds is not high enough to be measured. Type I diamonds are further divided into the types Ia and Ib. In ~~type~~ Ia diamonds~~,~~ nitrogen occurs in small aggregates, whereas type Ib contains isolated single nitrogen atoms at concentrations up to 500 ppm. Type II diamonds are also divided into two more types: IIa and IIb. IIa diamonds contain no measurable nitrogen or boron impurities and IIb diamonds are characterized by boron impurities which are considered to be isolated substitutional atoms[10][3].

2.1.2 Nanodiamond

In this thesis, two different kinds of diamonds have been examined: the Bulk diamond and the Nanodiamond. The term 'nanodiamond' describes diamonds with a thickness of less than a couple hundreds of nanometers. Nanodiamonds are mostly created via detonation, but synthesis methods also include ion and Laser bombarding, Chemical Vapour Deposition as well as ultrasonic, hydrothermal and electro-chemical techniques[6][24], ~~whereas Bulk diamonds are produced under high pressure and high temperature (HPHT) conditions.~~ NVs in the Bulk diamond are mainly influenced by the surrounding spin bath and are unaffected by surface structures. NVs in a nanodiamond on the other hand are additionally influenced by surface effects and therefore behave differently.

2.2 Physical properties of the NV defect center

A nitrogen-vacancy-center consists of a nitrogen atom (N) replacing a carbon atom, which is located next to a vacancy (V) in the diamond crystal lattice. There have been found two different types of NV-centers so far: the neutral NV^0 state and the negatively charged NV^- state where an additional electron is captured from the diamond lattice. Due to its well-known and useful optical properties, only latter has been the subject of interest in this work. Therefore it will just be referred to as NV in the following.

The NV is a model quantum system. It is optically stable, showing neither photo-

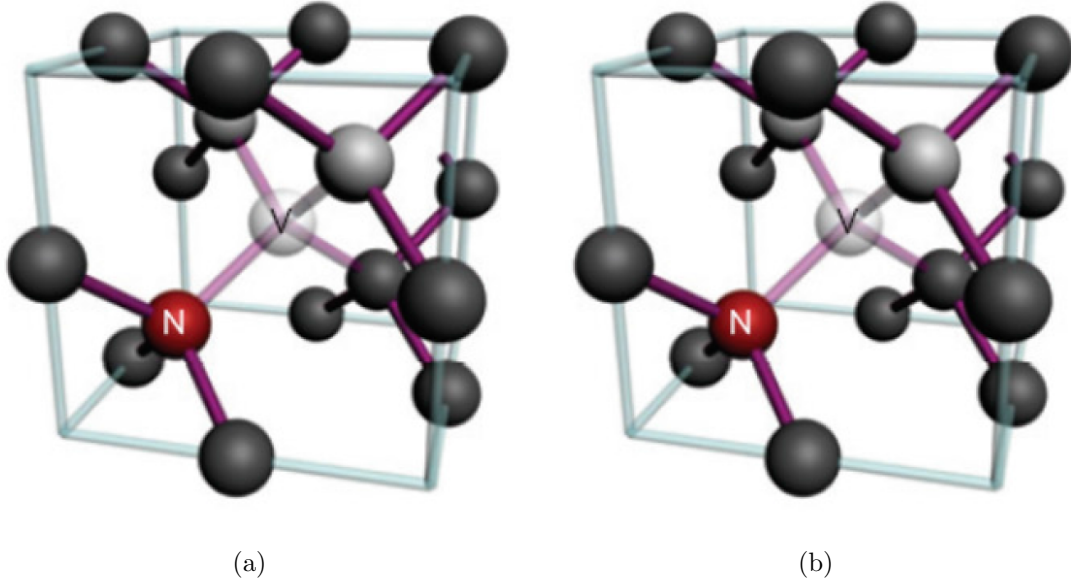<div align="center">(a)</div> <div align="center">(b)</div>

Figure 1: Figure (a) shows the structure of an NV-center in the diamond lattice, on the left one can see an autocorrelation measurement on an NV-center

blinking nor photobleaching, and achieves extraordinary coherence times. Furthermore, its spin state can be optically initialized and read out as it emits in the visible light range where high efficiency detectors are available. Another striking property is its single photon character which makes it useful in quantum computation and quantum cryptography and allows us to identify an NV using a photon correlation setup. A typical autocorrelation measurement is depicted in picture 2.2. A three-level system can be used to describe the optical properties of an NV. By using linear combination of atomic orbitals (LCAO)[18], an optical ground state ^3A having three spin sublevels is identified. The $m_s = 0$ and $m_s = \pm 1$ sublevels are separated by $\nu_{0\pm 1} = 2.87$ GHz when no magnetic field is applied. Two spin conserving optical dipole transitions connect the ground state with the first optical excited state ^3E. After being excited, the nitrogen vacancy can radiatively relax back to the ^3A level, producing broadband photoluminescence (PL) with a zero-phonon line at 637 nm. Another possible de-excitation path is the non radiative relaxation, that occours via intersystem crossing (ISC) to a singlet state ^1A. The ISCs to the singlet state are strongly spin selective as they have a higher probability to involve transitions from the $m_s = \pm 1$ sublevels than from $m_s = 0$. Furthermore, from the ^1A state, the decay rate to the $m_s = 0$ sublevel is much higher than to $m_s = \pm 1$. These spin-selective relaxation processes form the basis for optical detection of magnetic resonance (ODMR), as a change of the spin state will lead to a different fluores-

cence intensity from the defect center, the highest intensity being detected for the pure $m_s = 0$ state. Additionally, optical pumping ~~therefore~~ allows a high degree of $m_s = 0$ spin polarization. Consequently, if a resonant magnetic field is applied to an optically pumped NV, one observes a drop in PL intensity. Furthermore, when the NV is placed in a static magnetic field, the Zeeman effect leads to a lifting of the $m_s = \pm 1$ degeneracy, resulting in two resonance lines in the ESR spectrum. This makes it also possible to use an NV as a magnetic sensor on an atomic scale.

2.3 Second order correlation function

NVs are single photon sources. This means, that a single NV can only emit one photon at a time. After the emission, the system needs to be driven back to the excited state, which takes an initialization time in the order of μs, and after a relaxation time of a couple ns, it is able to emit a photon again. As a result, the intensity correlation function of an NV shows a characteristic behaviour and is helpful for identifying an NV.

The intensity correlation function of the light can be found by making two intensity measurements with a fixed time delay τ and averaging the product of the readings. As the normalized form of this function is more useful, the *degree of second-order temporal coherence* is defined as

$$g^{(2)}(\tau) = \frac{\langle \bar{I}(t)\bar{I}(t+\tau)\rangle}{\bar{I}^2} = \frac{\langle E^*(t)E^*(t+\tau)E(t+\tau)E(t)\rangle}{\langle E^*(t)E(t)\rangle^2} \tag{1}$$

where $\bar{I}$ is the averaged intensity[20]. For a single-mode light field, the coherence function at $\tau = 0$ can be expressed in terms of the *destruction* and *creation operators*:

$$g^{(2)}(0) = \frac{\langle \hat{a}^\dagger \hat{a}^\dagger \hat{a} \hat{a}\rangle}{\langle \hat{a}^\dagger \hat{a}\rangle^2} \tag{2}$$

Considering that $[\hat{a}, \hat{a}^\dagger] = 1$ and $\hat{n} = \hat{a}^\dagger \hat{a}$, one gets:

$$g^{(2)}(0) = \frac{\langle n^2\rangle - \langle n\rangle}{\langle n\rangle^2} \tag{3}$$

A single photon source can be described with a Fock state, for which $\langle n\rangle = n$ and $\langle n^2\rangle = n^2$, so that follows:

$$g^{(2)}(0) = 1 - \frac{1}{n} \tag{4}$$

2.4 Bloch notation

Dependent on the given problem, it is helpful to work with an appropriate notation. So, in order to describe the behaviour of a two-level system, the Bloch notation turns out to be ~~rather~~ practical.

An arbitrary state of a two-level system can be written as:

$$|\psi\rangle = \alpha|1\rangle + \beta|0\rangle = \alpha \begin{pmatrix} 1 \\ 0 \end{pmatrix} + \beta \begin{pmatrix} 0 \\ 1 \end{pmatrix} = \begin{pmatrix} \alpha \\ \beta \end{pmatrix} \tag{5}$$

where $|1\rangle$ and $|0\rangle$ are two orthogonal vectors representing the pure states. Taking into account the normalization condition $\langle\psi|\psi\rangle = |\alpha|^2 + |\beta|^2 = 1$, and neglecting a global phase without physical significance, one can rewrite this as:

$$|\psi\rangle = \cos\frac{\theta}{2}|1\rangle + e^{i\phi}\sin\frac{\theta}{2}|0\rangle \tag{6}$$

by introducing the angles θ and ϕ. Thus, an arbitrary state can be represented as a unitary vector on the Bloch sphere, a 3-D unit sphere, as shown in picture...
This notation will be used in the following to describe spin manipulations.

2.5 Rabi Oscillations

The notations in (5) and (6) can be used to describe a single spin in free space. By placing the single spin in a static magnetic field, the degenerate energy levels split up with E_0 and E_1 being the corresponding energies to the ground state $|0\rangle$ and the excited state $|1\rangle$. Working in the basis of the two eigenstates, the unperturbed Hamiltonian can then be written as:

$$\hat{H}_0 = \begin{pmatrix} E_1 & 0 \\ 0 & E_0 \end{pmatrix} = \frac{\hbar\omega_{10}}{2}\hat{\sigma}_z \tag{7}$$

with $\hbar\omega_{10} = E_1 - E_0$ and σ_z being the Pauli matrix which is introduced to simplify the equation. If the system is placed in an oscillatory magnetic field of the form [1]:

$$\hat{B} = B_1(\hat{x}\cos\omega t - \hat{y}\sin\omega t) \tag{8}$$

the interaction Hamiltonian reads:

$$\hat{H}_B = -\hat{\mu}\hat{B} = -\gamma\hat{B}\hat{S} = -\gamma B_1(\hat{S}_x\cos\omega t - \hat{S}_y\sin\omega t) \tag{9}$$

where $\hat{\mu}$ and γ are the magnetic moment and gyromagnetic ratio of the system, and $\hat{S}$ is the spin operator. Expressing the spin components through the Pauli matrices using $\hat{S}_i = \frac{\hbar}{2}\hat{\sigma}_i$, we finally obtain:

$$\hat{H}_B = -\gamma\frac{\hbar}{2}\left(B_1(\cos\omega t\hat{\sigma}_x - \sin\omega t\hat{\sigma}_y)\right) \tag{10}$$

This yields for the total Hamiltonian:

$$\hat{H} = \hat{H}_0 + \hat{H}_B = \begin{pmatrix} \frac{\hbar\omega_{10}}{2} & -\gamma\frac{\hbar}{2}B_1(\cos\omega t + i\sin\omega t) \\ -\gamma\frac{\hbar}{2}B_1(\cos\omega t - i\sin\omega t) & -\frac{\hbar\omega_{10}}{2} \end{pmatrix} \tag{11}$$

For simplicity, we introduce the larmor frequency $\omega_1 = \gamma B_1$ and express the oscillating terms using the complex exponential function:

$$\hat{H} = \frac{\hbar}{2}\begin{pmatrix} \omega_{10} & -\omega_1 e^{i\omega t} \\ -\omega_1 e^{-i\omega t} & -\omega_{10} \end{pmatrix} \tag{12}$$

For $\omega_{10} \gg \omega_1$, the eigenstates of the Hamiltonian remain basically unchanged. This allows us to use perturbation theory for the further investigation of the behaviour of the system.

The coefficients from equation (5) are now time-dependent and have to fulfil the following relations[16]:

$$\dot{\alpha} = -\frac{i}{\hbar} H'_{01} e^{-i\omega_{10}t} \beta, \qquad \dot{\beta} = -\frac{i}{\hbar} H'_{10} e^{i\omega_{10}t} \alpha \tag{13}$$

if the diagonal elements of the perturbation Hamiltonian H' are zero. This translates into a second order differential equation:

$$\ddot{\alpha} = -\frac{1}{\hbar^2} H'_{01} H'_{10} \alpha - i\omega_{10}\dot{\alpha} + \frac{1}{H'_{01}} \frac{\partial H'_{01}}{\partial t} \dot{\alpha} \tag{14}$$

With $H'_{01} = H'^*_{10} = -\frac{\hbar\omega_1}{2} e^{i\omega t}$, we get

$$\ddot{\alpha} - i(\omega - \omega_{10})\dot{\alpha} + \frac{\omega_1^2}{4}\alpha = 0 \tag{15}$$

Using the ansatz $\alpha = e^{\lambda t}$, we find:

$$\lambda_\pm = \frac{i}{2}\left(\omega - \omega_{10} \pm \sqrt{(\omega - \omega_{10})^2 + \omega_1^2}\right) \tag{16}$$

This gives us the general solution:

$$\alpha(t) = c_1 e^{\lambda_+ t} + c_2 e^{\lambda_- t} \tag{17}$$

Let the system be in state $|1\rangle$ at $t = 0$, providing the initial conditions $\alpha(0) = 1$ and $\beta(0) = 0$ and thereby giving the final result for $\alpha(t)$:

$$\alpha(t) = -\frac{\lambda_-}{\lambda_+ - \lambda_-} e^{\lambda_+ t} + \frac{\lambda_+}{\lambda_+ - \lambda_-} e^{\lambda_- t} \tag{18}$$

Now, the probability of the system going to state $|0\rangle$ can be found using the normalization condition:

$$P_{1 \to 0}(t) = |\beta(t)|^2 = 1 - |\alpha(t)|^2 = \frac{-2\lambda_+ \lambda_-}{(\lambda_+ - \lambda_-)^2} \sin^2\left(\frac{(\lambda_+ - \lambda_-)t}{2}\right) \tag{19}$$

Putting in the values of $\lambda_\pm$, we find:

$$P_{1 \to 0}(t) = \frac{\omega_1^2}{(\omega - \omega_{10})^2 - \omega_1^2} \sin^2\left(\frac{\sqrt{(\omega - \omega_{10})^2 - \omega_1^2}}{2} t\right) \tag{20}$$

This result is known as Rabi's formula.

When the frequency of the oscillating field B_1 equals the energy separation between the two states, $\omega_{10} = \omega_{01} = \omega$, the resonant condition is satisfied and the transition probability is simplified as:

$$P_{1 \to 0}(t) = \sin^2\left(\frac{\omega_1 t}{2}\right) \tag{21}$$

So for a magnetic pulse of length $\omega_1 t = \pi \Leftrightarrow t = \pi/\omega_1$ the system undergoes a complete transition from the ground state to the excited state. This corresponds to a rotation on the Bloch sphere by an angle of π and is hence called a π pulse. Applying a pulse of only half this length creates a coherent superposition of both states of equal weight, comparable to a rotation by the angle $\pi/2$ and therefore called $\pi/2$ pulse.

The above described phenomenon is very useful for the examination of NVs, for example when performing an RF scan. This is done by tuning a microwave over a range of about 100 MHz around the resonance frequency $\nu_{0\pm1} = 2.87\,\text{GHz}$ and measuring the intensity at the same time. The scan will result in a curve with one resonance dip at $\nu = \nu_{0\pm1}$ or two dips around that frequency, if the ground state sublevels of the NV are split. So, looking for a resonant frequency in this range is a reliable way to identify an NV. Furthermore, identifying the resonant frequency is essential for other ways of spin manipulation, as described below.

2.6 Density matrix

Until now any interaction process between the two level system and the external environment has been neglected. In order to take these phenomena into account, we may take advantage of the density matrix formalism. Here, a density operator can be defined as:

$$\hat{\rho} = |\psi(t)\rangle\langle\psi(t)| \tag{22}$$

Keeping the notation from equation 5, this gives for a two-level system:

$$\hat{\rho} = \begin{pmatrix} |\alpha|^2 & \alpha\beta^* \\ \beta\alpha^* & |\beta|^2 \end{pmatrix} \tag{23}$$

The diagonal elements are equivalent to the probabilities of finding the system in its eigenstates $|0\rangle$ or $|1\rangle$. Therefore, they are called *populations* and it is $\rho_{11} + \rho_{22} = 1$. The off-diagonal elements are called *coherences*[19].
From the Schrödinger equation we obtain[9]

$$i\hbar\frac{\partial\hat{\rho}}{\partial t} = [\hat{H}, \hat{\rho}] \tag{24}$$

In order to take the relaxation processes caused by the environment into account, we introduce the decay rate Γ from the excited state to the ground state. Using equation (24) we can now write in terms of the density matrix:

$$\frac{1}{i\hbar}[\hat{H}_R, \hat{\rho}]_{11} = \frac{-\rho_{11}}{T_1} = -\Gamma\rho_{11} \tag{25}$$

$$\frac{1}{i\hbar}[\hat{H}_R, \hat{\rho}]_{22} = \frac{\rho_{11}}{T_1} = (1 - \rho_{22})\Gamma \tag{26}$$

where $\hat{H}_R$ is the relaxation Hamiltonian and T_1 denotes the lifetime of the excited state and is known as *longitudinal relaxation*. As relaxation needs to be taken into account for the coherences as well, we additionally get

$$\frac{1}{i\hbar}[\hat{H}_R, \hat{\rho}]_{12} = \frac{-\rho_{12}}{T_{12}} = -\gamma\rho_{12} \tag{27}$$

$$\frac{1}{i\hbar}[\hat{H}_R, \hat{\rho}]_{21} = \frac{-\rho_{21}}{T_{21}} = -\gamma\rho_{21} \tag{28}$$

This process is called *transverse relaxation* with the relaxation time $T_{12} = T_{21} = T_2 = \gamma^{-1}$. In order to consider dephasing as well, we introduce the *dephasing time* T_2^* which is the transverse relaxation time modified by a dephasing time. It is [8]

$$2T_1 \geq T_2 \geq T_2^* \tag{29}$$

and for systems with an infinite ground state lifetime and no dephasing, the transverse and longitudinal relaxation are related through

$$\gamma = \frac{1}{2}\Gamma \tag{30}$$

These relaxation processes prevent the system from getting back to the initial amplitude, even if it's excited with a resonant frequency. The observed signal for Rabi oscillations is therefore not a sine but a convolution of a sine with the exponential function.

2.7 Spin manipulation sequences

As described in section 2.5, the spin state of a two-level system can be manipulated by applying a microwave pulse. A concatenation of multiple pulses is called a pulse sequence. In order to examine different NVs and prolong their coherence times, different types of sequences have come to use. The sequences have in common, that they all start with a laser pulse to initiate the system to $m_s = 0$ before the spin manipulation is performed.

2.7.1 Rabi Sequence

The Rabi sequence was used to determine the length of the π-pulse for a specific NV. So the sequence consists of a laser pulse which is long enough to initiate the system to $m_s = 0$ and a RF pulse of length τ. After that, the PL is measured. Measuring the PL for different lengths τ of the MW pulses yields an image of the Rabi Oscillations: An extremum is reached when τ matches a multiple of the length of a π pulse. Therefore, the time interval between two consecutive extrema gives the length of a π pulse for this NV.

2.7.2 Hahn Echo

In the Hahn Echo, a $\pi/2$ pulse is applied to create a coherent superposition of $m_s = 0$ and $m_s = 1$. This state can then evolute over a time τ and inhomogeneities of the magnetic field lead to dephasing. Then, a π pulse turns the polarization around and the same inhomogeneities refocus the spins again. So, after another time interval τ, the intensity has reached a maximum again. This phenomenon is called a *spin echo*. At that point, a second $\pi/2$ pulse is applied to map the signal to the readout basis [14] and the PL is measured. As only the effects of static fields cancel each other out, time dependent fluctuations prevent the system from fully getting back to the initial state. For simple spin systems, the PL will decay exponentially with the time τ. The inverse decay rate of the PL thus equals the transverse relaxation time T_2, as dephasing effects are removed. So, the Hahn Echo pulse sequence allows us to determine the T_2 time.
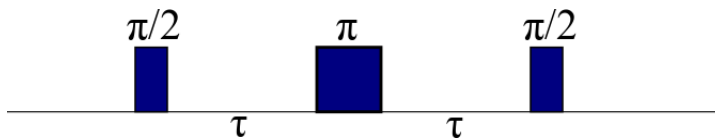

Figure 2: Hahn Echo sequence

2.7.3 Decoupling sequences

The surrounding spin bath of ^{13}C nuclei [7] is the main reason for dephasing of the NV spin and has a huge impact on the coherence time. This mechanism can be circumvented to some extent with specific sequences which decouple the NV spin from interactions with its environment and thereby increase the coherence times. In contrast to the Hahn Echo sequence, the spin echoes are here observed after the application of multiple pulses.

2.7.3.1 Carr-Purcell-Meiboom-Gill sequence The CPMG sequence begins with a $\pi/2$ rotation around the y axis, followed by a number n of $(\tau - \pi_x - \tau)$ pulses - τ being the relaxation time again - and ends with a $(-\pi/2)_y$ pulse, projecting the spin back to the bright state. The total relaxation time of the NV spin adds up to $T_{rel} = 2n\tau$. The CPMG-sequence can be seen as a succession of multiple Hahn Echoes. But whereas the Hahn Echo can only suppress fields which are constant over the durance of the whole sequence, CPMG can attenuate the influence of fields which are constant for at least 2τ, so also slowly varying inhomogeneities. As a consequence, sequences with more pulses should perform better.
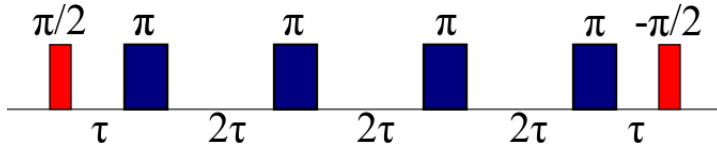

Figure 3: CPMG-4 sequence: red pulses represent rotations around the y-axis, blue pulses are rotations around the x-axis

2.7.3.2 XY sequence ~~As the name implies,~~ the XY sequences is made up of multiple π_x and π_y pulses. They are applied in two different variations: the asymmetric one, starting with an interval τ of free evolution and ending directly after the last pulse; and the symmetric one, which begins and ends with a $\tau/2$ interval. The symmetric sequences have been found to achieve longer coherence times[5][12] and were used in the experiments for this bachelor thesis. In general, the first half of the XY-sequence consists of $(\tau/2 - \pi_x - \tau - \pi_y - \tau/2)$ pulses and in the second part, the order is inverted and the sequence continues with the same number of $(\tau/2 - \pi_y - \tau - \pi_x - \tau/2)$ pulses. As before, the sequence is enclosed by two opposite $(\pi/2)_y$ pulses. With a number n of π pulses again, the total relaxation time turns out to be $T_{rel} = n\tau$. The advantage of XY-sequences compared to CPMG is their ability to refocus the spin with pulses along different spatial directions and therefore a better performance in the presence of a general, unknown interaction [7][4].
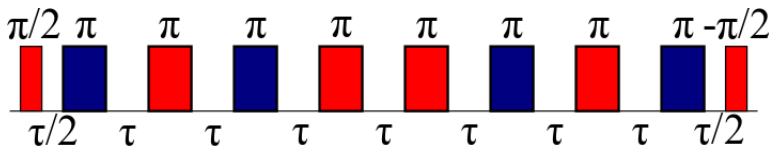

Figure 4: XY-8 sequence

2.7.3.3 UDD sequence ~~Interestingly,~~ equidistant pulse spacings do not always produce the best results with regard to decoupling. So, sequences with n π_x pulses

at the time points

$$\delta_j = \tau \sin^2\left(\frac{\pi j}{2n+2}\right) \tag{31}$$

have proven to achieve the optimum suppression of decoherence caused by imperfect pulses. Furthermore, they perform also well with regard to the decoupling from a spin bath [23]. Between the two required $(\pi/2)_y$ pulses, the sequence is symmetric with increasing time intervals to the middle and decreasing spacings to the end. The total free spin relaxation time of UDD is just τ.
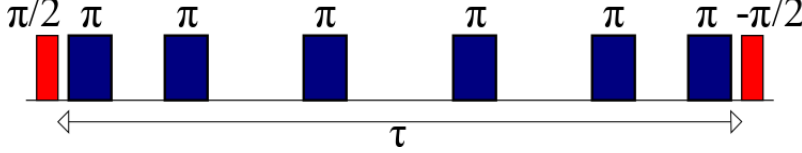

Figure 5: UDD-6 sequence

2.8 Spectral decomposition of the magnetic environment

For NV spins which are coupled to a magnetic environment, the loss of coherence can be generally described in the form [13]:

$$C(t) = e^{-\chi(t)} \tag{32}$$

where the decoherence functional is defined as

$$\chi(t) = \frac{1}{\pi}\int_0^\infty d\omega S(\omega)\frac{F(\omega t)}{\omega^2} \tag{33}$$

Here, $S(\omega)$ is the frequency-domain spectral density of the noise, thereby describing the coupling of the system to the environment, and $F_t(\omega)$ is the filter function that incorporates modulations being performed on the NV spins, for example in the form of a pulse sequence.
The dominant source of decoherence for the NV is a bath of randomly oriented N spins. Taking this into consideration, the spectral density of the noise can be assumed to be of Lorentzian shape:

$$S(\omega) = \frac{\Delta^2\tau_c}{\pi}\frac{1}{1+(\omega\tau_c)^2} \tag{34}$$

with the average coupling strength Δ of the spin bath to the probed NVs and the correlation time τ_c of the N bath spins with each other which is associated to their characteristic flip-flop time. With n_{spin} being the N bath density, it is expected that $\Delta \propto \tau_c^{-1} \propto n_{spin}$ [13].
The filter functions for the single-axis pulse sequences used in the experiments look as follows [11]:

$$\text{Hahn Echo} \qquad\qquad F(z) = 8\sin^4\left(\frac{z}{4}\right) \tag{35}$$

$$\text{CPMG} \qquad F(z) = 8\sin^4\left(\frac{z}{4n}\right)\sin^2\left(\frac{z}{2}\right)/\cos^2\left(\frac{z}{2n}\right) \tag{36}$$

$$\text{UDD} \qquad F(z) = \frac{1}{2}\left|\sum_{k=-n-1}^{n}(-1)^k\exp\left(\frac{iz}{2}\cos\left(\frac{\pi k}{n+1}\right)\right)\right|^2 \tag{37}$$

11

~~A filter function for XY could not be found, so these data can not be further evaluated.~~

With these filter functions and the assumption of a Lorentzian spin bath, each data point will yield values for Δ and τ_c, providing an image of the NV's magnetic environment.

A different approach can be made in the case $F(\omega t)/(\omega^2 t) = \delta(\omega - \omega_0)$. Then, the integral for $\chi(t)$ simply reduces to:

$$\chi(t) = tS(\omega_0)/\pi \tag{38}$$

thus rendering for the spectral function at frequency ω_0[13]:

$$S(\omega_0) = -\pi \ln(C(t))/t \tag{39}$$

3 Experimental realization

In the following section will be explained how the experiment was implemented and prepared. After describing the ~~general~~ setup, the principle of confocal microscopy will be discussed further, ~~because it was essential for the type of measurements we wanted to conduct.~~ At the end, the calibration of the components will be briefly commented.

3.1 Experimental setup

3.1.1 Optical setup

The first component of the setup is a 532 nm Laser that drives the NVs to $m_s = 0$. The Laser can be pulsed with an AOM with rise/fall times of approximately 50 ns. After that, the light goes through a 532 nm shortpass, creating a beam of the preferred wavelength. The next element is a dichroic mirror (DM) which reflects light above 600 nm and transmits light below that wavelength. Having passed the DM, the beam goes into the microscope and gets focused onto the sample with an objective lens of NA=1.35. The sample is a diamond with multiple NVs and is mounted onto a piezo-controlled xyz stage that allows the adjustment of the sample-to-objective distance. A microwave antenna is placed above the sample, allowing us to conduct ESR measurements and run decoupling sequences. The photons emitted by the NVs are collected with the lens before leaving the microscope. At the DM, the red PL gets reflected. A long pass filter removes residual Laser light, before the beam goes into the confocal part that is made up of two collecting lenses and a pinhole in between. At the end, the light reaches the APD and gets detected. Ideally, the last part of the setup would be a Hanbury-Brown-Twiss (HBT) setup to make autocorrelation measurements. This consists of a beam splitter, which has a 50:50 probability of either reflecting or transmitting the photons, and two APDs for counting the reflected and transmitted photons, respectively. This arrangement is also shown in the conceptual setup scheme.

Since the APD signals shouldn't be acquired all the time the APDs are gated. This means, that the detected intensity is only read out, when the gates are open. There are two gates: the reference gate (ref), which is open before the spin manipulation took place and the signal gate (sig) which is open at the end of the sequence. Their quotient sig/ref yields the normalized intensity.

The laser and the APD gates are controlled by a bit pattern generator with a minimum pulse length of 6.6 ns.

3.1.2 Microwave setup

For the purpose of doing various ESR measurements on the NVs, it was essential to use two different microwaves with a relative phase shift of 90°. This could be accomplished in an additional part of the setup. At first, the signal of the RF generator gets into a 0°-90° RF power splitter. Then, each separate signal goes through a switch that is controlled via TTL pulses from the bit pattern generator. Finally, the signals from both switches are recombined in a simple RF power combiner and transmitted to the microwave antenna. A setup scheme is depicted in figure 6
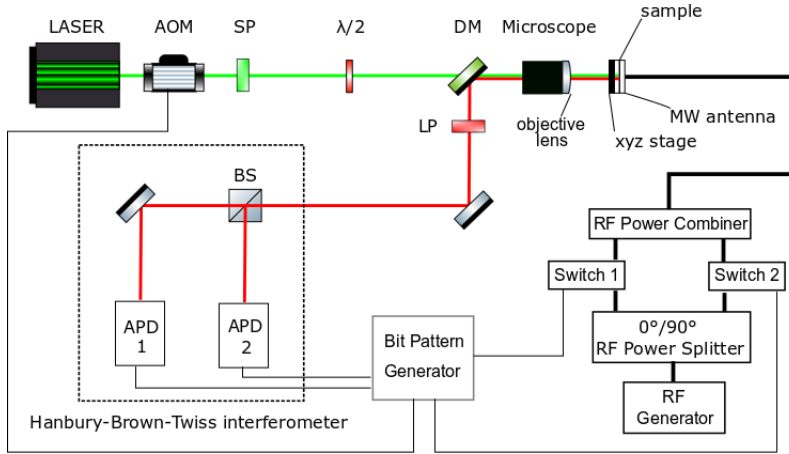

Figure 6: Schematic image of the conceptual experimental setup: Instead of the HBT part, the actual setup just contains an APD

3.2 Confocal microscopy

A conventional microscope collects all the light which is emitted or reflected by the sample, regardless of whether it originates from the focal plane or not and thus leading to a reduction in contrast and sharpness of the image. The ~~great~~ advantage of a confocal microscope is, that it doesn't only achieve a high 2-D resolution but is also able to suppress light which doesn't come from the focal plane. This can be achieved with a pinhole in a confocal plane. In our setup, it was implemented by putting two ~~collecting~~ lenses in the beam path and placing the pinhole in the mutual focal plane between the two lenses. As only the photons that go through the pinhole are detected, light from below or above the focal plane is extinguished. So, this arrangement accomplishes depth discrimination as shown in figure 7.
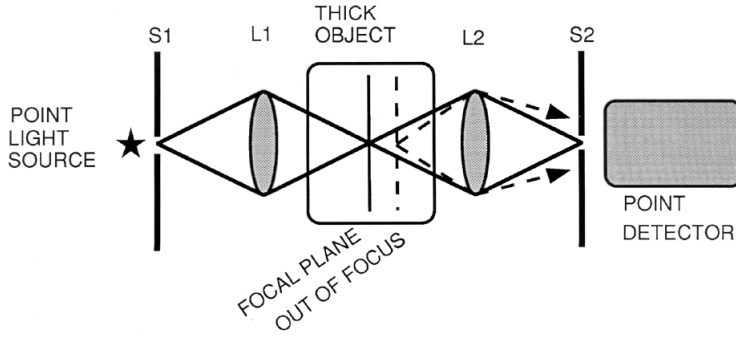
Figure 7: Schematic image of the confocal part of the setup, illustrating depth discrimination with the dashed beams. This image was taken from [21]

Obviously, the degree of depth discrimination depends on the size of the pinhole and can consequently be modified by changing the diameter of this aperture. However, in our experiments only the smallest possible hole was used. Furthermore, the confocal part also filters out stray light, hence enhancing the contrast[15].

3.2.1 Point Spread Function

Due to diffraction effects, light that comes from a point-like object in the focal plane doesn't converge to a single point in the image plane. It rather spreads slightly in all directions, even in a diffraction-limited system, where all optical components have ideal properties and are perfectly adjusted. In confocal fluorescence microscopy, this phenomenon occurs actually twice: the laser light cannot be ideally focused onto the sample, and the emitted light cannot be perfectly focused on the pinhole. The image of a single point can be described by the point spread function (PSF), which accordingly contains information about the highest possible resolution. Since the confocal microscope enables imaging in three dimensions, it is necessary to consider the 3-D PSF, which appears to be a rotational ellipsoid:

Figure 8: Slices through the 3-D PSF. The left image shows the intensity distribution in axial direction and the right image shows a lateral plane. These images were taken from[15]

According to the Rayleigh-criterion, "two components of equal intensity should be considered to be just resolved when the principal intensity maximum of one coincides with the first intensity minimum of the other"[2]. Naturally, resolution is also affected by the signal-to-noise ratio of the system[22], so this criterion cannot be

applied in every case. The distance to the first minimum can be conveniently approximated with the *full width at half maximum* (FWHM) of the distribution, so this property will be employed to determine the resolution. Considering the limited resolving power of the objective lens, described by its numerical aperture NA, it is

$$FWHM_z \approx \frac{0.88 \cdot \lambda_{exc}}{\left(n - \sqrt{n^2 - (NA)^2}\right)} \tag{40}$$

for the axial confocal PSF and we get

$$FWHM_{xy} \approx 0.51 \frac{\lambda_{exc}}{NA} \tag{41}$$

for the lateral resolution with λ_{exc} being the excitation wavelength and n the refractive index of the immersion medium. These formulae were derived assuming that the pinhole is large compared to the diameter of the Airy disc,

$$PH \gg \frac{1.22 \cdot \sqrt{\lambda_{exc} \cdot \lambda_{em}}}{NA} \tag{42}$$

with the emission wavelength λ_{em}, so that additional diffraction could be neglected[15]. After inserting the numbers, equation 42 becomes

$$PH \gg 526.1 \, \text{nm} \tag{43}$$

which is well satisfied for the pinhole diameter of 50 μm. So, one gets for the resolution

$$FWHM_z \approx 568 \, \text{nm} \tag{44}$$

and

$$FWHM_{xy} \approx 201 \, \text{nm} \tag{45}$$

3.3   Calibration

Owing to various lengths of wires and inherent distinctions between the components of the setup, the signals of the bit pattern generator (BPG) don't get to all components at the same time and need different amounts of time to be processed. Consequently, the sequence which is output by the BPG is executed in a completely different way, making it essential to adjust the timing of each element. As just the relative delays of the components to each other needed to be adapted, the delay of the laser was set to zero and the other delays were determined with respect to the laser.

3.3.1   Calibration of the gates

To calibrate the gates, the microscope had to be focused on an NV. Then, the laser was switched on for a short period of time, thereby exciting the NV and producing fluorescence. Simultaneously, the signal and reference gates detected the intensity over the same timespan but with different delays regarding the laser. Thus, the maximum of intensity could be observed when excitation and detection window synchronized, providing the corresponding delay time.
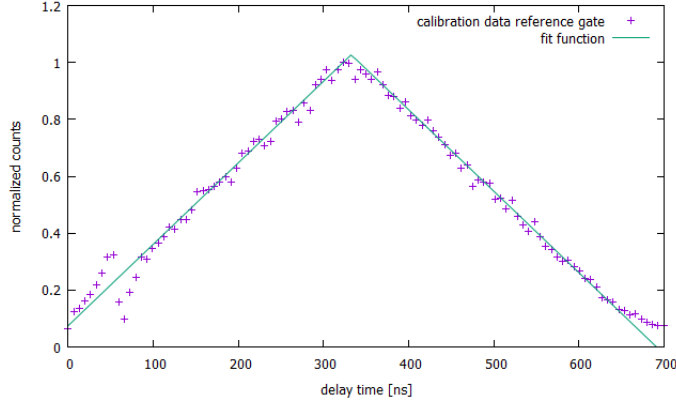
15

Figure 9: Measurement of the normalized intensity(divided by the maximum value) in dependence of the gate position regarding the laser; the peak of the graph yields the time delay

3.3.2 calibration of the microwaves

For the calibration of the microwaves, the laser was turned on for the duration T of the sequence, driving the NV to $m_s = 1$. Additionally, a MW pulse of length τ was applied at time t, the reference was measured from $T/2 - \tau$ until $T/2$ and the signal directly after that, from $T/2$ to $T/2 + \tau$. Then, the signals were measured for different t from 0 to $T - \tau$, shifting the pulse through the sequence. For small t, the normalized intensity would be 1, as the NV is driven back to the excited state by the laser. When t increases further, the counts measured in the reference gate decrease, resulting in a normalized intensity above 1. When the microwave pulse is exactly between the two gates, the normalized intensity reaches 1 again and afterwards, the image is the same as before, just vice versa. So, the microwave is timed correctly, when the normalized intensity goes to 1 exactly at $T/2$.
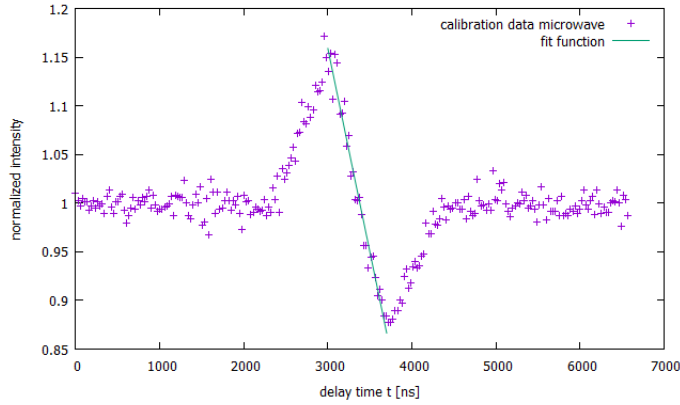

Figure 10: Measurement of the normalized intensity as a function of the mw pulse position

4 Measurements

In order to lift the degeneration of the $m_s = \pm 1$ sublevel of the NV, a static magnet was placed near the sample. Each set of measurements started with an RF scan.

16

For the ensuing measurements it was necessary to determine the resonant frequencies as accurately as possible. Therefore, the RF scan data were fit with a double-Lorentzian function. The RF scan was followed by the Rabi sequence. So as to make sure that both microwaves had the same power, the Rabi sequence was performed with each MW phase separately. As mentioned in section 2.6, the data were fit with a product function of sine and cosine. After that, a Hahn Echo was acquired to determine the dephasing time without decoupling pulses. Then, the decoupling sequences could be executed.

4.1 Examination of the Nanodiamond

The first measurements were conducted on the Nanodiamond. With an NV density of about 10 per $(\mu m)^2$, we were able to focus the microscope on single NVs and study their properties.

4.1.1 Finding an NV and determining a resonant frequency

The process of finding a suitable NV for the measurement included focussing on multiple NVs and making RF scans. When the contrast was sufficiently high - meaning an intensity difference of at least 15% during the scan - and the resonance dips were more than 50 MHz apart and therefore easily separable, the NV could be considered suitable. So, for the first suitable NV we got the following image: Theoretically, the performance of the decoupling sequences should be identical for
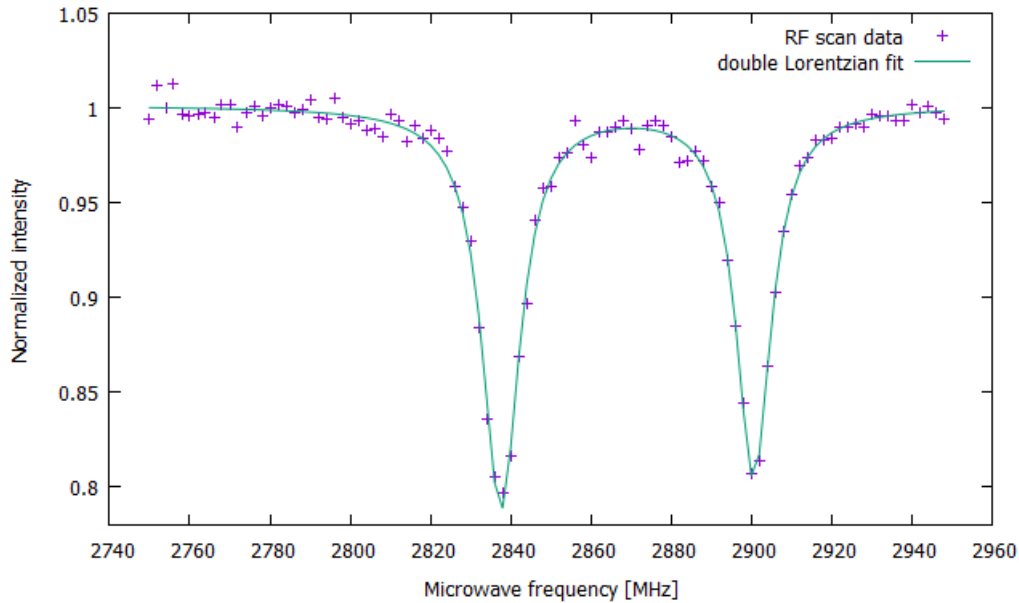

Figure 11: Rf scan, showing a separation of 60 MHz of the resonant transitions. The data were fit with a double-Lorentzian

the $m_s = +1$ and $m_s = -1$ sublevel. Consequently, the resonance frequency can be chosen at will and measurements with both resonance frequencies would be futile because the data sets would be almost identical.
~~As the first resonance dip has about 1% more contrast, the $m_s = -1$ transition will be examined.~~ From the fit, we get $\nu_{0-1} = 2837.5\,\mathrm{MHz}$.

4.1.2 Finding pi pulse length and measuring T_2

From the corresponding Rabi oscillations(figure 12) one gets the $\pi/2$ pulse length $t_{\pi/2} = 182\,\text{ns}$.
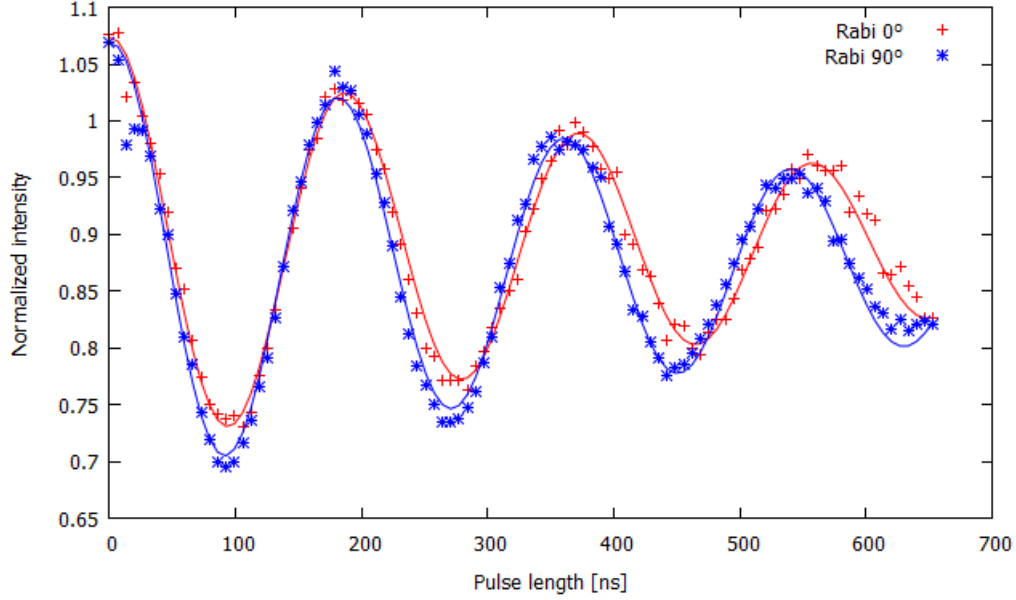

Figure 12: Rabi oscillations for normal and phase-shifted MW

With this knowledge, spin manipulation measurements could now be executed. The exponential decay of the spin echoes was fit with an exponential function of the form

$$I(t) = c_1 e^{-\left(\frac{t}{t_0}\right)^{\alpha}} + c_2 \tag{46}$$
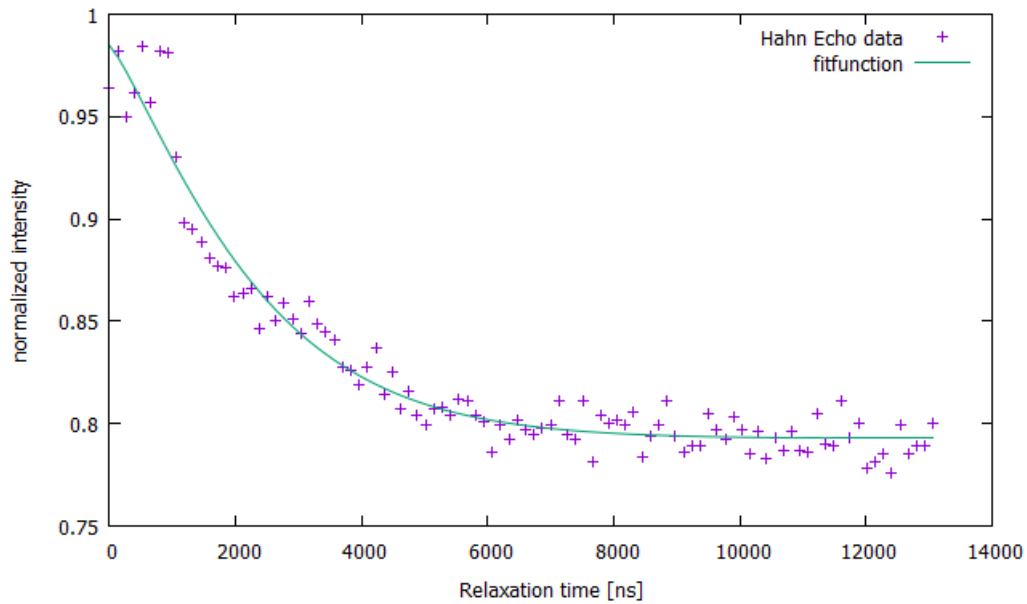
with t_0 being the coherence time.

Figure 13: Hahn Echo

18

The Hahn Echo (figure 13) gives for the relaxation time $T_2 = t_0 = 2.41 \pm 0.12\,\mu s$. ~~The value $\alpha = (1.2 \pm 0.1)$ indicates the expected exponential behaviour.~~

4.1.3 ==decoupling== sequences

The setup only allowed to apply 0° or 90° microwave pulses. Consequently, instead of a final ==$-\pi/2$== pulse, we could only generate a $3\pi/2$ pulse to project the spin onto the bright state. Another ==possibility== was to end the sequence with ~~just~~ another $\pi/2$ pulse which would project the spin onto the dark state of the NV. The advantage of this approach is that the last MW pulse is much shorter and the pulse errors have a smaller impact on the measurement, resulting in a higher contrast. ~~That is why the sequences were implemented with only a $\pi/2$ pulse at the end.~~ Considering that the populations of bright and dark state are inverted with respect to each other, the behaviour of the data curves will also be inverted to what one would get using the correct realization of the sequences. ==But the readout basis can be chosen at will, so this is just== a matter of convenience and doesn't change the physical meaning of the measurements.

4.1.3.1 CPMG
The CPMG-sequence has been examined for 8, 16, 32 and 64 π pulses. It would have been possible to do measurements with less pulses, but as the shortest symmetric XY-sequence is XY-8, the data wouldn't have been comparable to other sequences.
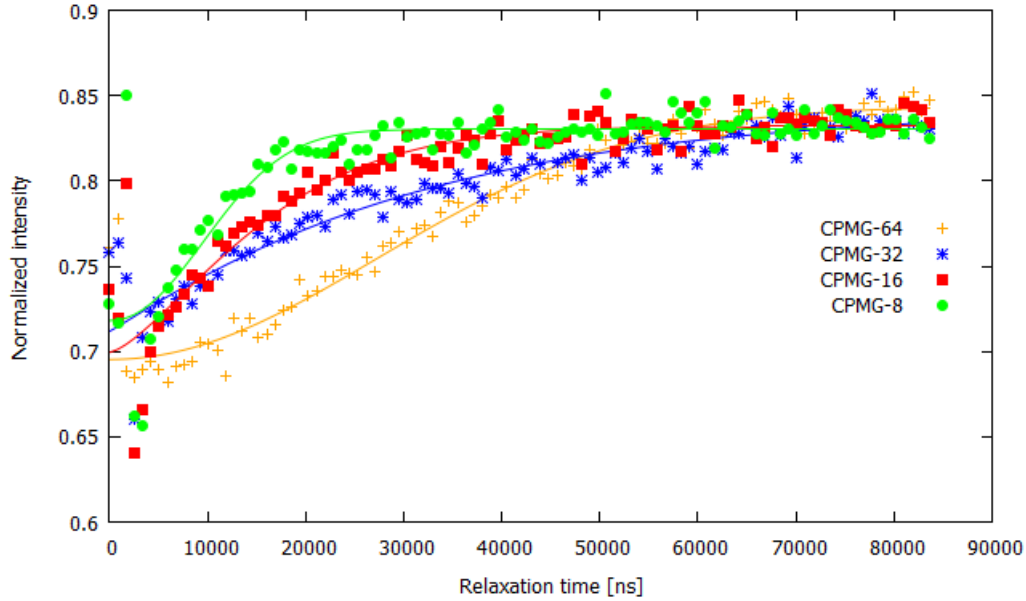

Figure 14: Comparison of CPMG-sequences with different numbers of pulses. The data have been fit with an exponential function as described in equation 46. It can be seen that the coherence time increases with the number of pulses

From a qualitative point of view, the curves (figure14) show the expected behaviour: the more pulses are applied, the ==slower decays the intensity. The quantitative analysis, however, shows a different result(table 1).== ==In theory, the exponent α should increase with the number of pulses, because the system stays longer in the $m_s = 0$ state.== Apparently, the theory doesn't hold for the measurements: the first

3 sequences actually show a contradictory behaviour with a decreasing value of α. Only from 32 to 64 pulses does α increase, but is still below the value for 8 pulses. Apart from that does the coherence time show the predicted behaviour: it rises gradually with the number of π-pulses and gets as far as almost 16 times the relaxation time.

Table 1: Exponential behaviour and coherence times for different numbers of pulses

sequence	exponent α	t_0 [ns]	t_0/T_2
CPMG-8	2.13 ± 0.53	12880 ± 1066	5.35
CPMG-16	1.42 ± 0.22	17483 ± 1389	7.26
CPMG-32	1.06 ± 0.19	31654 ± 3682	13.14
CPMG-64	2.03 ± 0.17	38053 ± 1178	15.80

The fact that there are several configurations of NVs in the Nanodiamond - each with different physical properties - requires the examination of multiple NVs in order to get a representative result. Furthermore, one has to assume that the performance of decoupling sequences depends on the particular NV.

From Hahn Echoes of various NVs, we got transverse relaxation times T_2 in the range between 250 ns and 2.5 ms. The CPMG sequence was conducted for NVs with $0.9\,\text{ms} \leq T_2 \leq 2.4\,\text{ms}$ (figure 15).
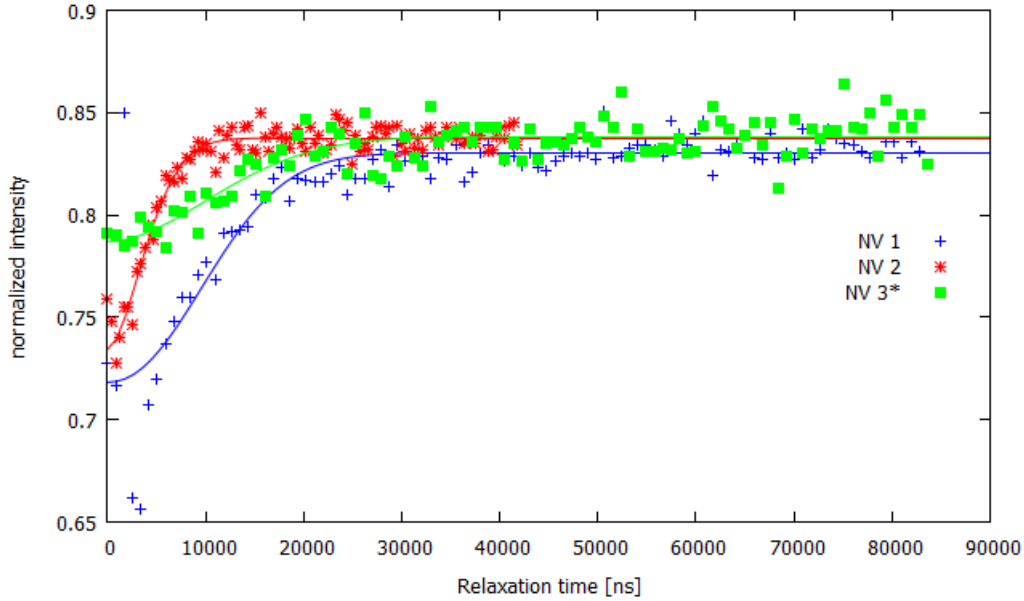

Figure 15: Comparison of CPMG-8 sequences for different NVs with T_2 times ranging from 0.9 ms (NV 3) to 2.4 ms (NV 1). For a better comparability, the data of NV 3 were modified by an offset of 0.1. The data have been fit with an exponential function as described in equation 46.

It can be seen that the same decoupling sequence achieves different coherence times depending on the specific properties of the NV. The contrast seems to have no effect on the performance of the sequence.

Table 2: Exponential behaviour and coherence times of CPMG-8 for different NVs

	exponent α	t_0 [ns]	t_0/T_2
NV 1	2.13 ± 0.53	12900 ± 1100	5.35
NV 2	1.76 ± 0.17	5000 ± 200	3.45
NV 3	1.89 ± 0.49	14700 ± 1400	16.63

The fit data(table 2) exhibit a consistency with regard to the exponential be-
haviour: all values of α lie within a range of 0.4 around 2. This allows to say that
CPMG-8 has an in general unchanged effect on a random NV.
The development of the coherence times under CPMG-8 manipulation is less consis-
tent. All coherence times are increasing, but the extent of the enhancement varies
greatly. The quotient of coherence and the NV's T_2 time, representing something
like a "degree of decoupling", ranges from 3.5 to over 16 and thereby differs by a fac-
tor 5. This underlines the previously stated dependency of the decoupling efficiency
on the individual properties of the NV.

4.1.3.2 XY
Analogously to CPMG, The XY-sequence has been performed with 8, 16, 32 and 64
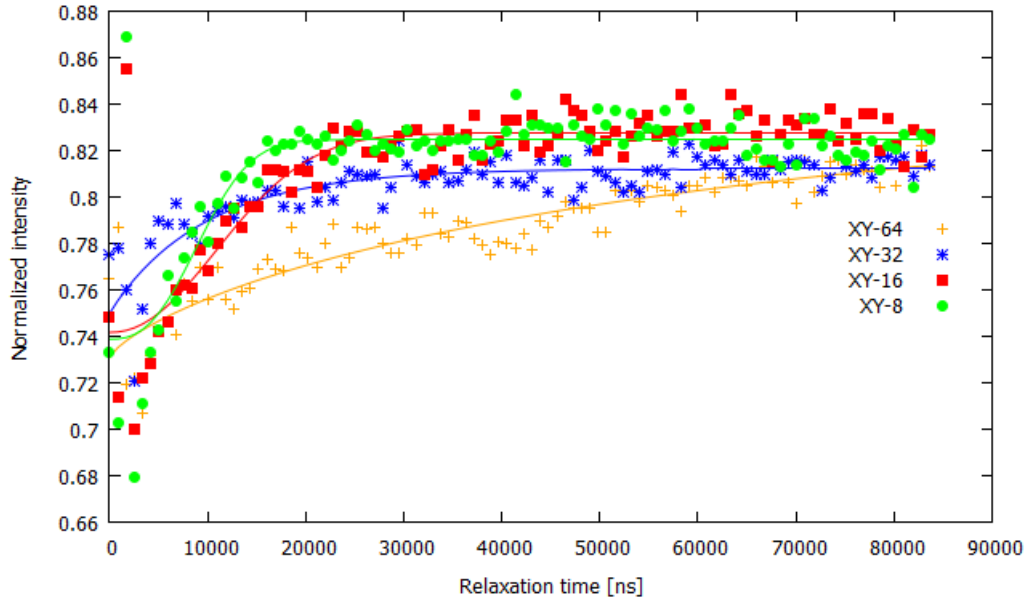pulses.

Figure 16: Comparison of the XY-sequence for different numbers of π pulses. The
sequence with 16 pulses has improved the coherence time with respect to XY-8.
The sequences with more pulses deviate from this trend and show an abnormal
behaviour. The data have been fit with an exponential function as described in
equation 46.

The plot shows that XY-8 and XY-16 behave similarly as the CPMG sequences
with the same numbers of pulses. However, the tendency doesn't continue for higher
numbers of pulses: XY-32 and XY-64 exhibit great discrepancies regarding the se-
quences with fewer pulses. This is also underlined by the fit parameters. The first
two sequences could achieve an improvement up to 6 times the T_2 time, but re-
garding the huge error for $t_0(XY-64)$, this is the best that could be accomplished

with XY sequences for ==this== NV. Furthermore, the decreasing exponent α has been observed as well for CMPG, ==so the theoretical predictions don't fit to the results for α.==

Table 3: Exponential behaviour and coherence times for XY

sequence	exponent α	t_0 [ns]	t_0/T_2
XY-8	2.62 ± 0.91	10700 ± 1000	4.42
XY-16	2.14 ± 0.54	14600 ± 1200	6.07
XY-32	0.97 ± 0.26	9800 ± 2200	4.06
XY-64	0.76 ± 0.34	65000 ± 70000	26.92

Taking a closer look at XY-64, the curve seems to be composed out of two different exponential functions: in the beginning, the function decays up to a relaxation time of about 40 μs. After that, a second, ~~steeper~~ decay ==starts.==
This behaviour indicates an external influence apart from the spin bath that drives the NV, as it was observed for the Bulk diamond. So, for a second evaluation, the exponential function was just fit in the interval from 0 to 40 4μs.
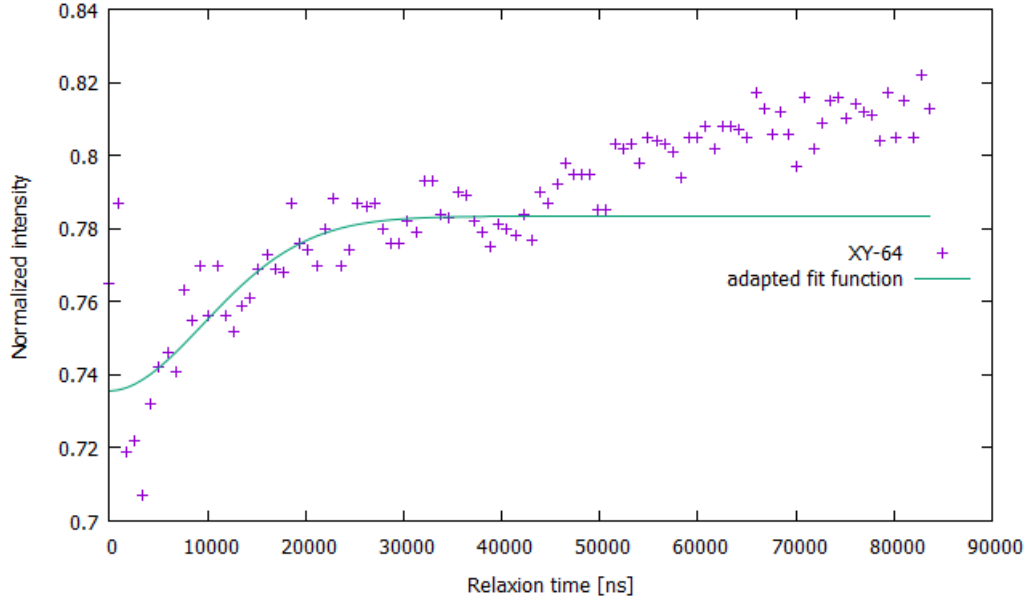

Figure 17: Fit of the XY-64 data with an unchanged function but a shorter interval ending at 40 μs relaxation time. The first curvature could be better approximated with the fit function than in figure (16)

The second fit gives a relaxation time of $t_0 = 14000 \pm 2000$ ns. This is no improvement towards XY-16, but confirms the trend that XY with more than 16 pulses doesn't get any better. In conclusion, XY sequences can't improve the relaxation time by more than a factor 6 for this NV.

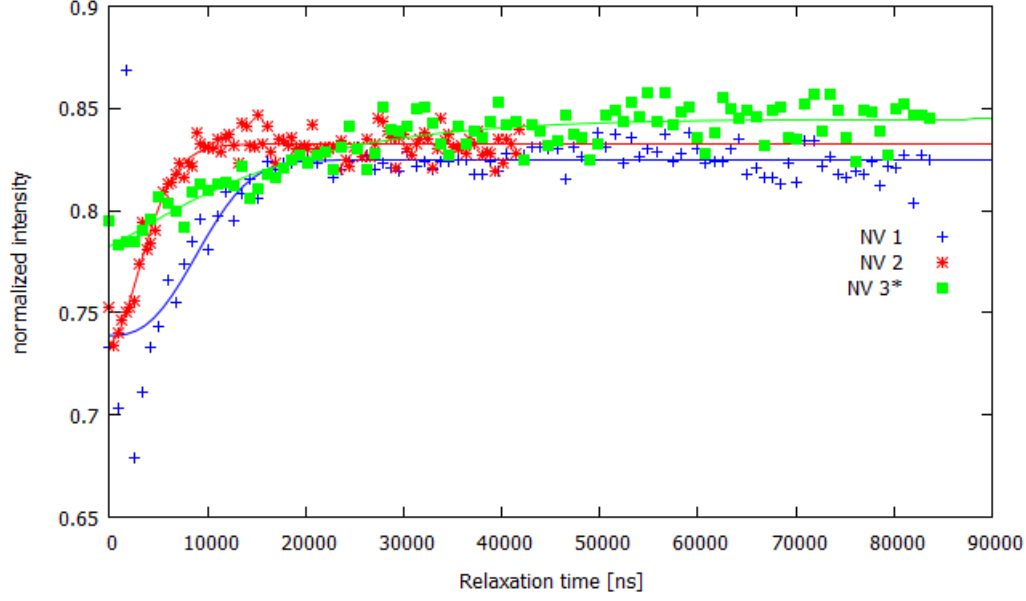The comparison of XY-8 for different NVs ==is not much different from CPMG-8.==

Figure 18: Comparison of XY-8 sequences for different NVs with T_2 times ranging from 0.9 ms (NV 3) to 2.4 ms (NV 1). Again, the data of NV 3 were modified by an offset of 0.1. The data have been fit with an exponential function as described in equation 46.

In fact, XY-8 performs best for NV 3, as it was the case for CPMG-8. Here, an improvement of factor 19 could be accomplished. For the other NVs, XY-8 gave slightly worse results for the T_2 time.

Table 4: Fit parameters of XY-8 for different NVs

	exponent α	t_0 [ns]	t_0/T_2
NV 1	2.62 ± 0.90	10700 ± 1000	4.42
NV 2	1.74 ± 0.20	4600 ± 200	3.18
NV 3	1.15 ± 0.24	17000 ± 2000	19.42

All in all, this means that the success of decoupling depends in particular on the NV and only to little extent on the chosen decoupling sequence.

4.1.3.3 UDD

~~The application of UDD pulse sequences didn't work as well as CPMG and XY. Nonetheless, some successful measurements have been conducted.~~
~~To begin with,~~ the concrete way of implementing UDD allowed multiple interpretations. As CPMG and XY are characterized by equidistant pulse spacings, it makes no difference whether to consider the intervals between the edges of the pulses or between the centers of the pulses. This is not the case for UDD, because the intervals between consecutive π pulses are time dependent. For that reason, UDD was implemented in two ways. The first method had edge-to-edge spacings as described in paragraph 2.7.3.3 equation 31, the second one arranged the centers of pulses according to this relation. It should be remarked that both approaches are reasonable, because the derivation of the UDD pulse spacings is based on the assumption of perfect δ pulses [23]. Obviously, for $t(\pi) \to 0$, both options are equal, so the theory

The graph displays an enhancement of the relaxation time through UDD, actually almost similar to the effect of XY-8 and CPMG-8. The downside, however, are the great fluctuations of the data points even for long relaxation times. This effect intensifies further for sequences with more pulses, which is why only UDD with 8 pulses could be applied successfully. A possible reason for the great variation is the finite resolution of the pit pattern generator: the implementation of UDD gets incorrect, when the sinusoidal time intervals are rounded to multiples of 6.6 ns.
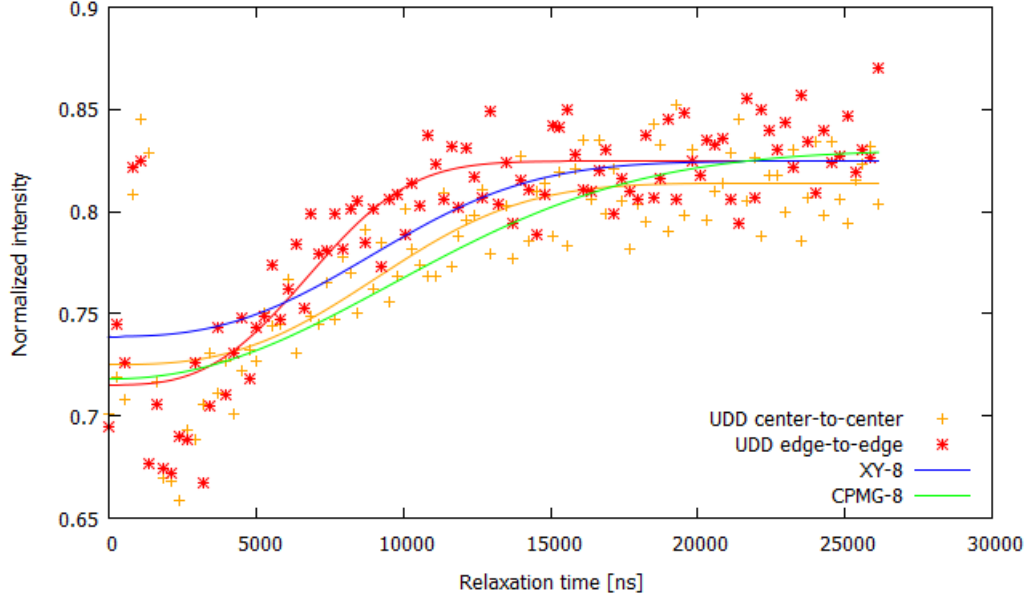

Figure 19: UDD-8 sequences in two different configurations. For comparison, the fit curves of XY-8 and CPMG-8 are included in the graph. The center-to-center pulse spacings achieve a higher coherence time than the second alternative. The improvement of T_2 is comparable to the other decoupling sequences, but the data points are scattered more widely. The data have been fit with an exponential function as described in equation 46.

It can be seen that UDD-8 with center-to-center pulse spacings accomplishes a higher coherence time than the second sequence. This is confirmed by the fit parameters (table 19): t_0 is almost 3 μs higher for the first implementation and even matches the value for XY-8.

Table 5: Comparison of both UDD-8 sequences with CPMG-8 and XY-8

	exponent α	t_0 [ns]	t_0/T_2
UDD-8 center-to-center	2.81 ± 0.90	10600 ± 900	4.39
UDD-8 edge-to-edge	2.95 ± 0.80	7700 ± 500	3.22
CPMG-8	2.13 ± 0.53	12900 ± 1100	5.35
XY-8	2.62 ± 0.90	10700 ± 1000	4.42

In conclusion, one can say that UDD should be implemented with center-to-center pulse spacings and a better way to realize the exact timings.

24

4.1.4 Comparison of XY and CPMG

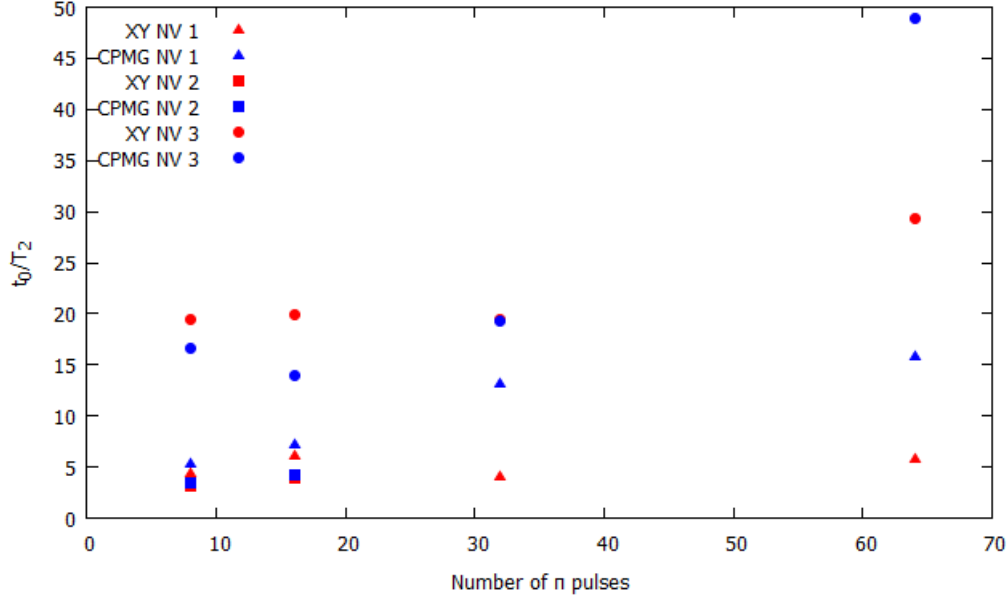It is now interesting to find out if this is also the case for Nanodiamonds.

Figure 20: Extension of the relaxation time, quantified by the quotient t_0/T_2, as a function of the number of π pulses for XY and CPMG sequences in different NVs. For 8 and 16 pulses, both sequences perform equally well; when more than 16 pulses are applied, CPMG gives better results, achieving an enhancement of up to 50 times T_2.

It turns out that both sequence types reach similar coherence times for 8 and 16 pulses, XY performing slightly better than CPMG for the third NV. Regarding the sequences with more pulses, CPMG could achieve longer coherence times than XY, even for NV 3, where the short sequences performed worse than XY.

4.2 Examination of the Bulk diamond

After the measurements on the Nanodiamond, the decoupling sequences should also be tested on a Bulk diamond. Because of the high NV density, it was now no longer possible to focus on single NVs. Instead, the behaviour of the whole spin bath was observed. Diamond having 4 principal crystal axes, the NVs can be oriented in 4 different spatial directions. Consequently, as it is not possible to choose a specific NV for the measurements, one will also get a signal from NVs which are not suitably aligned. The result is a reduced contrast with regard to the Nanodiamond.

4.2.1 Finding π pulse length and measuring T_2

The reduced contrast gets visible in the RF scan: while the Nanodiamond reached over 20% contrast, the Bulk diamond didn't even achieve half as much. The afore-mentioned 4 possible alignments of NVs should actually result in 8 resonance dips,

the $m_= \pm 1$ sublevels each splitting up differently according to their orientation. However, the scan only shows 2 dips similar to the Nanodiamond. This indicates that a significant amount of NV electron spins is well aligned with the magnetic field whereas the signal from the other NVs is suppressed by an imperfect orientation and he low contrast.
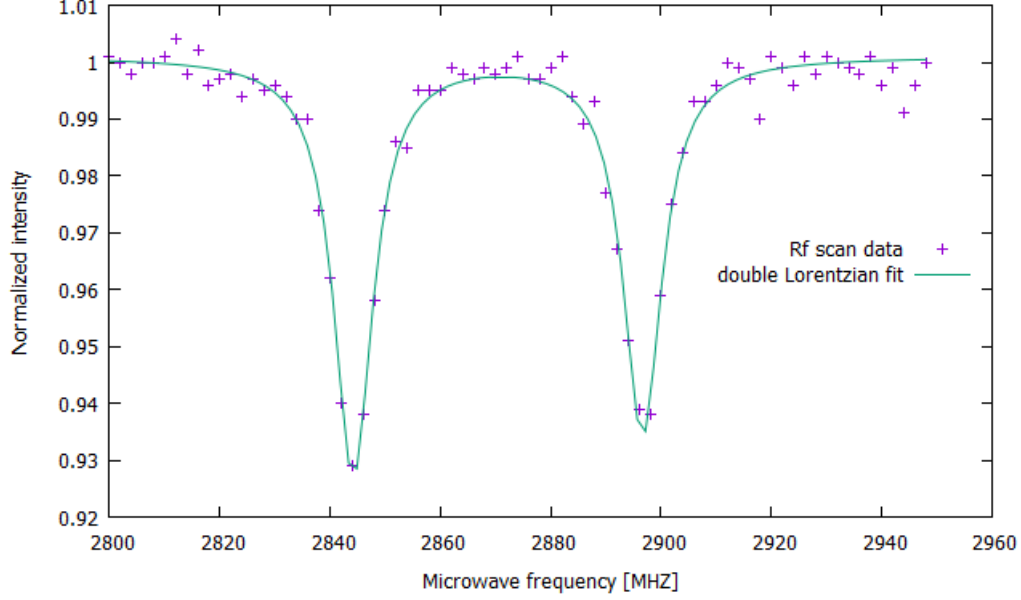

Figure 21: RF scan on the spin bath of the Bulk diamond, revealing two resonances separated by about 50 MHz.

For the decoupling sequences, the first resonant was chosen because of the higher contrast.

The conduct of Rabi oscillations (figure (22)) reveals a very high π pulse length of about 745 ns, which is 4 times as long as for the Nanodiamond measurement.
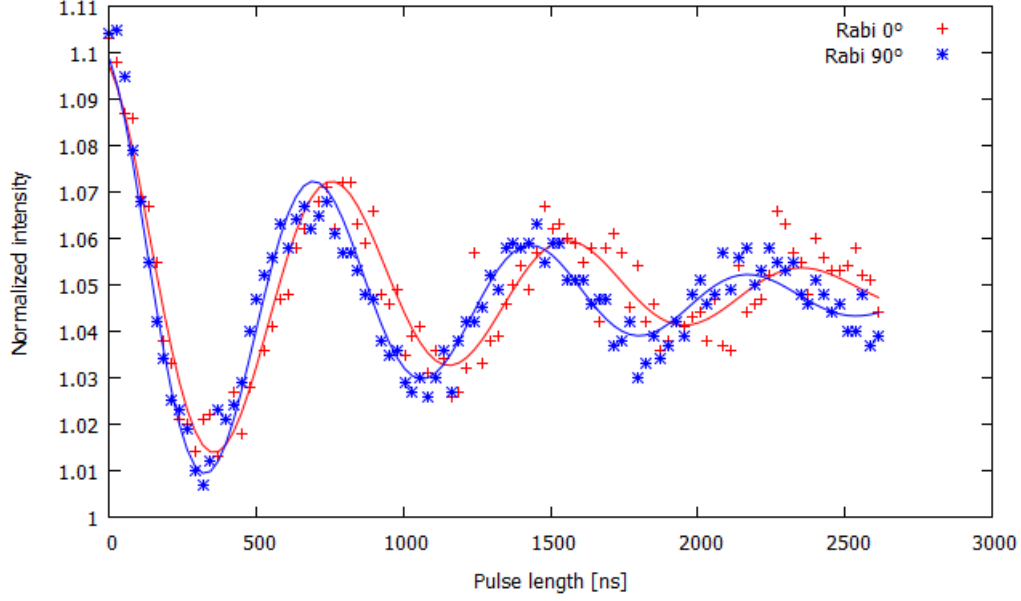
Figure 22: Rabi oscillations with both phases on the spin bath.

The corresponding Hahn Echo (figure (23)) exhibits a fast decay in comparison with the Nanodiamond. Furthermore, the relaxation is followed by an unexpected rise in intensity. The surrounding spin bath leading only to a relaxation of the spin, another mechanism seems to drive the system back to $m_s = 0$. This aspect will be discussed further during the evaluation of the decoupling sequences.
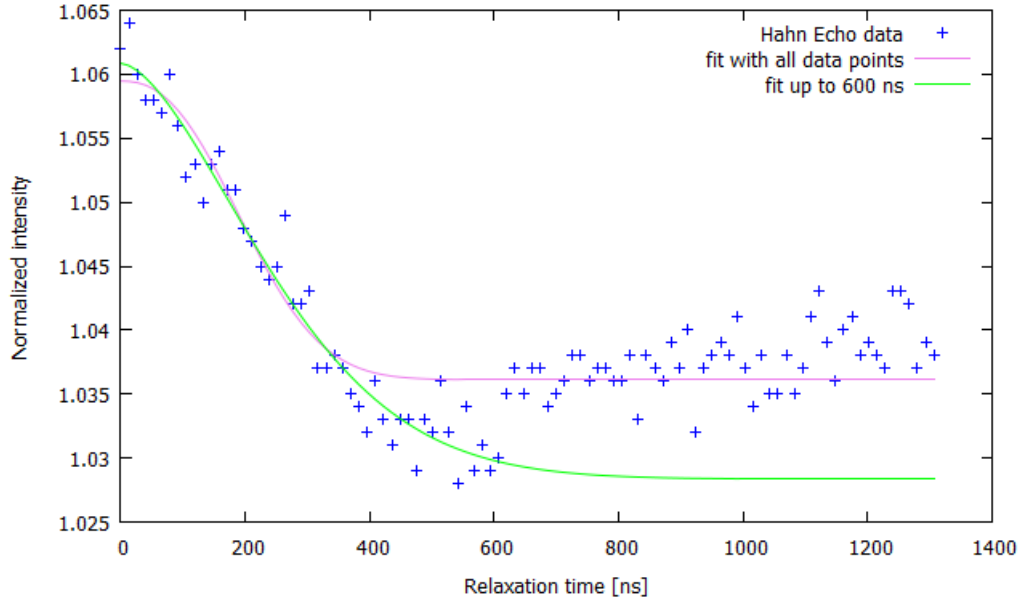

Figure 23: Hahn Echo for the Bulk diamond. After an initial decay, the intensity increases again, suggesting an external influence that drives the spin back to the bright state. For this reason, two different fits have been made: the first fit included all data points, the second one only the points which describe the actual decay that occurs for relaxation times below 600 ns.

The ordinary fit that factors in all data points results in a relaxation time of

27

$T_2 = 235 \pm 13\,\text{ns}$. <mark>Assuming</mark> that the increase of intensity is independent of the relaxation caused by the spin bath, an alternative fit has been made, excluding relaxation times of more than 600 ns. From that, one gets $T_2 = 302 \pm 25\,\text{ns}$. For the investigation of coherence time improvement through dynamical decoupling, the T_2 time acquired from the adjusted fit will be considered the actual relaxation time.

4.2.2 Decoupling sequences

In order to <mark>examine the extent of</mark> external driving, a reference measurement was done in addition to every scan. So, after the performance of dynamical decoupling, the same sequence was conducted with an off-set microwave, meaning a Rf frequency 100 MHz below resonance. As external driving and dynamical decoupling both cause an increase of intensity, the scans looked very similar. This is why also decoupling sequences with a finite $^{3\pi}/_2$ were implemented, because the effects of driving and dynamical decoupling would now compensate each other. An example of all 3 types of scans is shown in figure (24).
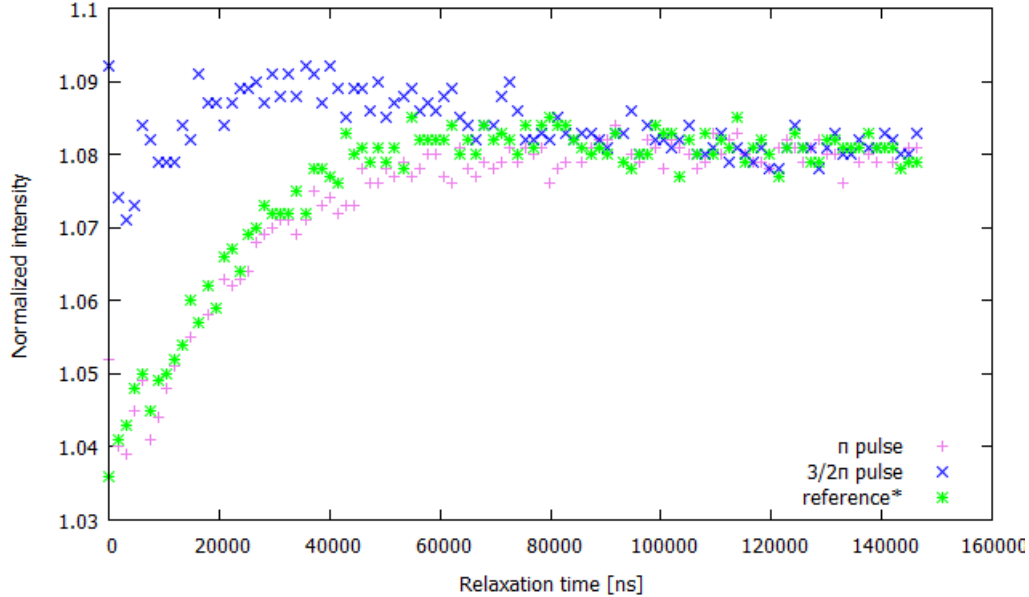

Figure 24: Examination of the driving for CPMG-16. The reference dataset was shifted by a constant for better comparison. The conventional measurement and the reference look almost similar; the sequence with a finite $3\pi/2$ pulse differs from the other two.

Getting meaningful data required to subtract the driving effect from the decoupling. For this, there were 3 obvious options: one could remove the background from either the conventional or the $3\pi/2$ measurement, or one could directly both decoupling measurements. Attempting to gain the highest possible contrast, latter has been done. <mark>Analogous to the visibility in interferometric experiments, the signal was determined vi</mark>a

$$I = \frac{I(3\pi/2) - I(\pi)}{I(3\pi/2) + I(\pi)} \tag{47}$$

for the decoupling sequences.

4.2.2.1 CPMG

Due to the low contrast, the decoupling sequences were only conducted up to a length of 32 pulses.
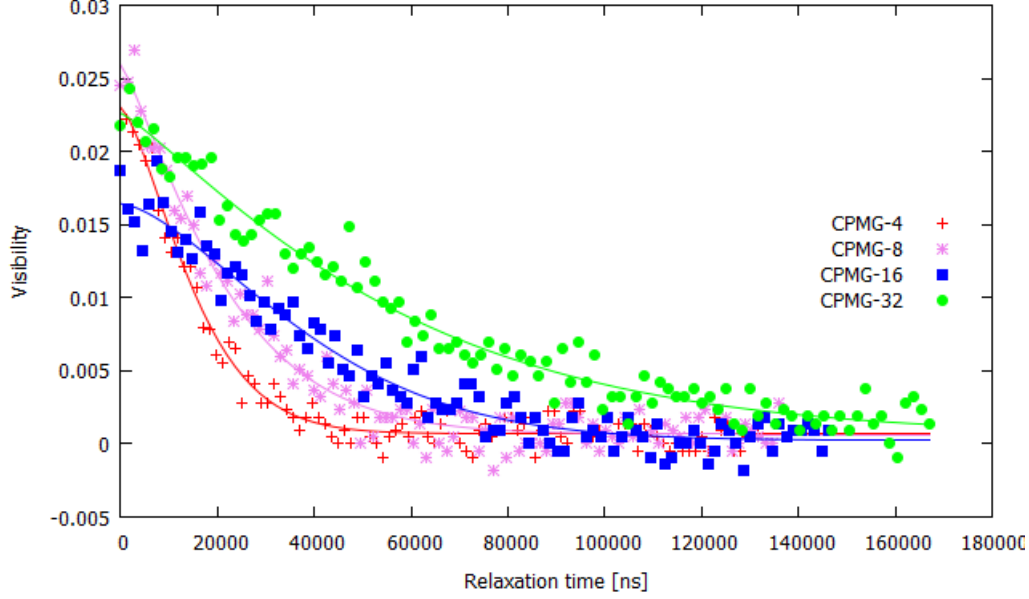

Figure 25: CPMG on the Bulk diamond for different numbers of pulses. A continuous increase of the cohernence time can be observed.

The plot (figure (25) shows that the coherence time gradually increases with the number of pulses. This gets also verified by the fit parameters (table (6). While α still shows no consistent behaviour, the coherence time rises up to 60 μs which corresponds to almost 200 times T_2.

Table 6: CPMG fit parameters for different numbers of π pulses

number of pulses	exponent α	coherence time [ns]	t_0/T_2
4	1.44$\pm$ 0.10	17200$\pm$ 700	57
8	1.22$\pm$ 0.10	23100$\pm$ 1100	77
16	1.54$\pm$ 0.15	44500$\pm$ 1900	148
32	1.17$\pm$ 0.11	59500$\pm$ 3100	197

Compared to the Nanodiamond, the improvement of coherence time has increased by almost an order of magnitude.

4.2.2.2 XY

Also the XY sequence was only conducted up to 32 pulses. The plot(figure 26) makes clear that all XY sequences on the spin bath give the same result. In conclusion, XY-8 already achieves the maximum coherence time possible with an XY pulse sequence for the spin bath. The fit data (table 7) support this observation: sequences with more pulses don't accomplish a distinct improvement of the T_2 time with respect to XY-8.
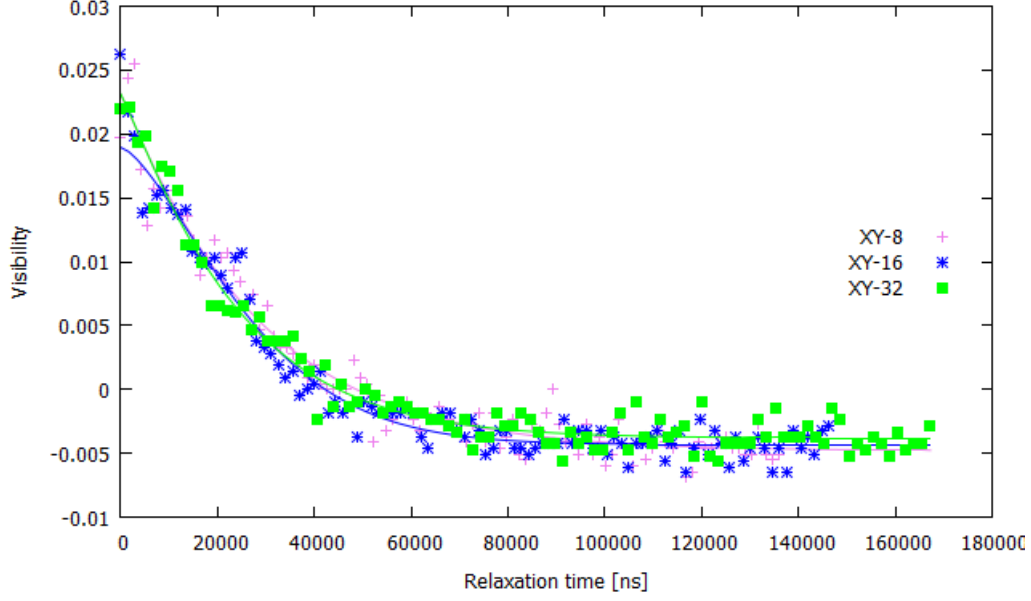
Figure 26: XY on the Bulk diamond for different numbers of pulses. All scans give almost similar results.

Table 7: XY fit parameters for different numbers of π pulses

number of pulses	exponent α	coherence time [ns]	t_0/T_2
8	1.02 ± 0.10	28500 ± 1700	94
16	1.46 ± 0.12	29600 ± 1200	98
32	1.11 ± 0.10	24500 ± 1400	81

4.2.2.3   Comparison of XY and CPMG   As shown before, CPMG gradually enhances the coherence time with an increasing number of pulses whereas XY-8 already achieves the highest coherence time for XY sequences. Consequently, if 8 pulses are applied, the XY gives better results than CPMG. However, when more pulses are applied, CPMG outperforms XY and reaches up to twice the coherence time.

Therefore, CPMG also realizes a better decoupling of the NV spin from the spin bath of a Bulk diamond.
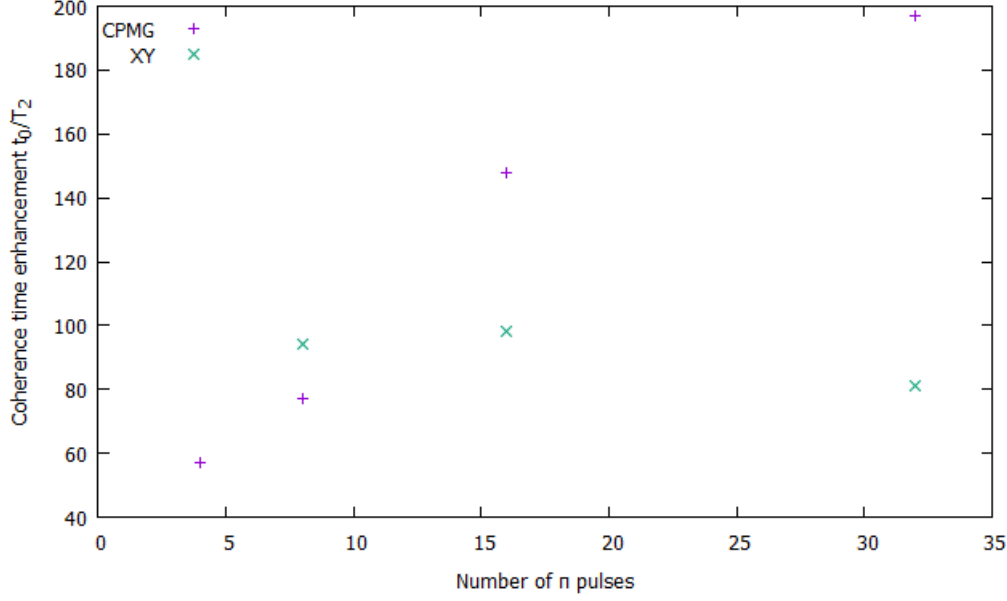
Figure 27: Comparison of XY and CPMG sequences on the spin bath

4.3 Comparison of Nanodiamond and Bulk diamond

For both the single NV electron spins in the Nanodiamond and the NV spin ensemble of the Bulk diamond, CPMG performed better than XY. While having prolonged the coherence time of a single spin by an order of magnitude, the T_2 time of the NV spin bath could be improved by more than two orders of magnitude. However, the achieved maximum coherence time was in both cases in the range of 50 μs, so this criterion favours neither Nanodiamond nor the Bulk. Considering the much higher contrast of the single electron spins, the Nanodiamond seems to be more suitable for magnetometry measurements.

References

[1] Michel Le Bellac. *A Short Introduction to Quantum Information and Quantum Computation*. Cambridge University Press, 2006.

[2] Max Born and Emil Wolf. *Principles of Optics*. Pergamon Press, 1970.

[3] Christopher M. Breeding and James E. Shigley. The "Type" Classification System of Diamonds and Its Importance in Gemology. *Gems & Gemology*, 2009.

[4] A. M. Souza et al. Robust dynamical decoupling. *Phil. Trans. R. Soc. A 2012 370*, 2011.

[5] Alexandre M. Souza et al. Effects of time-reversal symmetry in dynamical decoupling. *Physical Review A 85*, 2012.

[6] Boris I. Kharisov et al. Synthesis Techiques, Properties and Applications of Nanodiamonds. *Synthesis and Reactivity in Inorganic, Metal-Organic, and Nano-Metal Chemistry Vol. 40*, 2010.

[7] C. A. Ryan et al. Robust Decoupling Techniques to Extend Quantum Coherence in Diamond. *Physical Review Letters*, 2010.

[8] C. Lü et al. Spin relaxation time, spin dephasing time and ensemble spin dephasing time in n-type GaAs quantum wells. *Physics Letters*, 2007.

[9] Claude Cohen-Tannoudji et al. *Quantum mechanics*. WILEY, 1977.

[10] J. E. Field et al. *The Properties of Diamond*. Academic Press, 1979.

[11] L. Cywinski et al. How to enhance dephasing time in superconducting qubits. *Physical Review B 77*, 2008.

[12] M. A. A. Ahmed et al. Robustness of dynamical decoupling sequences. *arXiv:1211.5001v2*, 2012.

[13] N. Bar-Gill et al. Suppression of spin-bath dynamics for improved coherence of multi-spin-qubit systems. *Nature Communications 3, Article number: 858*, 2012.

[14] R. Hanson et al. Room-temperature manipulation and decoherence of a single spin in diamond. *Physical Review B 74*, 2006.

[15] Stefan Wilhelm et al. Die konfokale Laser Scanning Mikroskopie. Technical report, Carl Zeiss Mikroskopsysteme, 2003.

[16] David J. Griffiths. *Quantenmechanik*. Pearson, 2012.

[17] R. Gross and A. Marx. *Festkörperphysik*. De Gruyter, 2014.

[18] A. Lenef and S. C. Rand. Electronic structure of the NV-center in diamond: Theory. *Physical Review B 53*, 1996.

[19] Malcolm H. Levitt. *Spin dynamics*. WILEY, 2001.

[20] Rodney Loudon. *The quantum theory of light*. Oxford University Press, 2004.

[21] Barry R. Masters. *Confocal Microscopy and Multiphoton Excitation Microscopy: The Genesis of Live Cell Imaging*. SPIE Press, 2006.

[22] Michiel Müller. *Confocal Fluorescence Microscopy*. SPIE Press, 2006.

[23] Götz S. Uhrig. Exact Results on Dynamical Decoupling by Pi Pulses in Quantum Information Processes. *arXiv:0803.1427v2*, 2008.

[24] Oliver A. Williams. *Nanodiamond*. Cambridge: Royal Society of Chemistry, 2014.